International Journal of Heat and Mass Transfer 91 (2015) 908–921

Contents lists available at ScienceDirect

International Journal of Heat and Mass Transfer

journal homepage: www.elsevier.com/locate/ijhmt

On laminar natural convection inside multi-layered spherical shells

Yosef Gulberg, Yuri Feldman *

Department of Mechanical Engineering, Ben-Gurion University of the Negev, P.O. Box 653, Beer-Sheva 84105, Israel

ARTICLE INFO

Article history:
Received 11 January 2015
Received in revised form 2 July 2015
Accepted 7 July 2015
Available online 27 August 2015

Keywords:
Laminar natural convection
Multi-layered spherical shells
Nu–Ra functional relation
Immersed boundary method

ABSTRACT

Laminar natural convection flow inside multi-layered spherical shells with internal hot and external cold boundaries was investigated. Direct numerical simulations (DNS), which were performed by utilizing the immersed boundary method, addressed the fully 3D natural convection flow inside spherical shells with concentric, eccentric, equi-spaced and non-equi-spaced zero-thickness internal baffles. The insulation efficiency of the spherical shell was studied for up to four equi-spaced concentric internal layers. A unified functional dependency correlating modified Nu^* and Ra^* numbers was derived for spherical shells with up to four equi-spaced concentric internal layers. The effects of both vertical and horizontal eccentricity of the internal layers and of the width variation of concentric layers on the overall insulating performance of the spherical shell were investigated and quantified in terms of the *Nu–Ra* functionality.

1. Introduction

Buoyancy-driven flow developing inside spherical annuli has been the subject of considerable research, both theoretical and experimental for the past fifty years. Typically, the buoyancy-driven flow between two isothermal concentric spheres (where each sphere is held at a different temperature) has been investigated as a function of the diameter ratio, $\phi = D_i/D_o$, and the Rayleigh, *Ra*, and Prandtl, *Pr*, numbers. The pioneering experimental studies of Bishop et al. [1,2], which focused on visualization of the flow, indicated three distinct types of flow pattern – "crescent eddy", "kidney-shaped" and "falling vortices" – that depend on the diameter ratio, ϕ, of the shells. Their experimental results were confirmed by the study of Mack and Hardee [3], who derived a low-Rayleigh-numbers analytical solution for the natural convection of air between two concentric spheres. More recently, the natural convection flow of working fluids other than air (namely, water and silicone oils) was experimentally addressed by Scanlan et al. [4] and visualized by Yin et al.[5]. The later group described naturally induced flow patterns and categorized the type of the flow for each fluid in terms of the inverse of the relative gap width and the Rayleigh number. Subsequent numerical studies on steady and transient natural convection flow inside spherical shells extended the state of the art to an even wider range of *Pr* ($0.71 \leqslant Pr \leqslant 100$) [6,7] and *Ra* ($10^2 \leqslant Ra \leqslant 5 \times 10^5$) [7] numbers and to the analysis of vertically eccentric configurations [8].

The theoretical analysis of unsteady natural convection inside a differentially heated spherical annulus is a challenging problem, since different flow regimes can dominate locally in its different regions, taking the form of Rayleigh-Bènard convection at the top of the shell, of a differentially heated cavity at the near-equatorial region, and of a thermally stable flow regime at the bottom of the shell. Moreover, instabilities and transition scenarios are sensitive to the value of the *Pr* number and to the ratio of the internal to external diameter ϕ [9,10]. For shells with an internal hot boundary and an external cold boundary, the flow patterns vary with the ratio ϕ: Powe et al. [11] described a "modified kidney shaped eddy" for wide shells ($\phi \leqslant 0.5$), an "interior e xpansion–contraction" for $0.5 \leqslant \phi \leq 0.65$, a "three dimensional spiral" flow for $0.65 \leqslant \phi \leq 0.85$, and a "falling vortices" pattern for narrow shells ($0.85 \leqslant \phi$). Futterer et al. [12] reported that the flow inside shells of large and moderate widths ($0.41 \leqslant \phi \leq 0.71$) with a cold internal boundary and a hot external boundary exhibited an unsteady "dripping blob" phenomenon for $Pr = \infty$.

Natural convection inside a spherical annulus comprises an essential heat transfer mechanism in various engineering design problems, such as in solar energy collectors, storage tanks, thermal energy storage (TES) systems and nuclear reactors. Another potential application of spherical annuli is related to the design of the Titan Montgolfiere hot air balloon, which was recently chosen by NASA as the air-robot vehicle of choice for the exploration of Titan's atmosphere. Given Titan's low gravity (one-seventh that of Earth) and its cryogenic atmospheric temperatures (72–94 K), heat transfer by radiation can safely be neglected, and natural convection can be regarded as the only heat transfer mechanism for the stationary suspended balloon. Such a balloon, designed to

* Corresponding author.

http://dx.doi.org/10.1016/j.ijheatmasstransfer.2015.07.032
0017-9310/

provide a minimized heat flux rate through its walls, could serve as a sustainable air-robot platform for carrying a payload sufficient for a long-term space mission.

The concept of the double-walled Titan Montgolfiere, for which the spherical shell plays the role of a thermal insulator separating the hot interior of the balloon from the cold surroundings, has recently been established and investigated by Samanta et al. [13] and Feldman et al. [14]. One of the main findings of both studies was that theoretical estimation of the heat flux rate through the boundaries of the insulating gap of both scaled and full-scale balloons has the greatest uncertainties. This finding motivated further research [15], which was focussed on a more detailed analysis of transitional and fully turbulent natural convection flows inside narrow spherical differentially heated shells ($0.8 \leqslant \phi \leq 0.9$) and yielded an improved Nusselt (Nu)-Ra correlation derived specifically for that range of ϕ values.

The current study is aimed at further developing high-fidelity computational fluid dynamics (CFD) concepts for minimizing the heat flux rate through an insulating gap of spherical shape. In particular, the natural convection flow inside multi-layered differentially heated spherical shells with internal baffles of zero thickness is studied by DNS. The flow developing inside spherical shells characterized by both equi-spaced/non-equi-spaced and concentric/eccentric distributions of the internal baffles is simulated. The immersed boundary method (IBM) is utilized for treating the internal and external shell walls. Additionally, a novel modified $Nu^* - Ra^*$ correlation is derived for a spherical shell with up to four internal equi-spaced concentric layers in the range of $10^3 \leqslant Ra \leqslant 10^7$.

2. Physical model and governing equations

The natural convection flow inside single- or multi-layered spherical shells formulated in Cartesian coordinates (x,y,z) with the origin located at the center of the shell and gravity acting opposite to the positive direction of z axis (see Fig. 1) is governed by the following non-dimensional Navier–Stokes (NS) and energy equations:

$$\nabla \cdot \boldsymbol{u} = 0 \tag{1}$$

$$\frac{\partial \boldsymbol{u}}{\partial t} + (\boldsymbol{u} \cdot \nabla)\boldsymbol{u} = -\nabla p + \sqrt{\frac{Pr}{Ra}}\nabla^2 \boldsymbol{u} + \theta \vec{e}_z \tag{2}$$

$$\frac{\partial \theta}{\partial t} + (\boldsymbol{u} \cdot \nabla)\theta = \frac{1}{\sqrt{PrRa}}\nabla^2 \theta, \tag{3}$$

where $\boldsymbol{u} = (u,v,w)$, p, t, and θ are the non-dimensional velocity, pressure, time and temperature, respectively, and $\vec{e}_z$ is a unit vector in the vertical (z) direction. The Boussinesq approximation $\rho = \rho_0(1 - \beta(T - T_c))$ was applied to address the flow buoyancy effects. As a result, an additional temperature term appears as a source in the momentum equation in the z direction (see Eq. (2)), thereby allowing for the temperature–velocity coupling. The problem is scaled by L, $U = \sqrt{g\beta L \Delta T}$, $t = L/U$, and $P = \rho U^2$ for length, velocity, time, and pressure, respectively. Here, $L = R_o - R_i$ is the total shell width, defined as a difference between the outer, R_o and the inner R_i radius of the shell, ρ is the mass density, g is the gravitational acceleration, β is the isobaric coefficient of thermal expansion, and $\Delta T = T_h - T_c$ is the temperature difference between the hot and cold boundaries. The non-dimensional temperature θ is defined as $\theta = (T - T_c)/\Delta T$. The Ra and Pr numbers are $Ra = \frac{g\beta}{\nu\alpha}\Delta T L^3$ and $Pr = \nu/\alpha$, where ν is the kinematic viscosity and α is the thermal diffusivity. All the simulations were performed for the value of $Pr = 0.71$ corresponding to air.

The IBM [16] was implemented for imposing Dirichlet boundary conditions for the temperature and velocity fields at the spherical shell boundaries and the internal baffles. The IBM is not a standalone solver; rather, it requires a "driver" with which to be combined and its implementation should be perceived as a philosophy of enforcing boundary conditions. In principle, such a "driver" can be any time-marching solver, whose efficiency is typically boosted by choosing a computational domain of rectangular/prismatic shape and by utilizing a structured grid for spatial discretization of the NS and energy equations. In the present formulation the flow within the differentially heated spherical shell is an integral part of a more general natural convection flow within the whole cube, including also the outer ($R > R_o$) and the inner ($R < R_i$) regions (see Fig. 1). The flow was simulated by applying no-slip boundary conditions at all the cube faces, which were held at a constant temperature T_c (the same as the temperature of external boundary of the spherical shell). In the following, only the results relevant to the spherical shell region are discussed. Below, we detail the IBM formulation implemented in the present study.

Fig. 2 shows the setup of a typical spatial discretization implemented on a staggered grid. The grid is characterized by offset velocity, temperature and pressure fields. An immersed object of

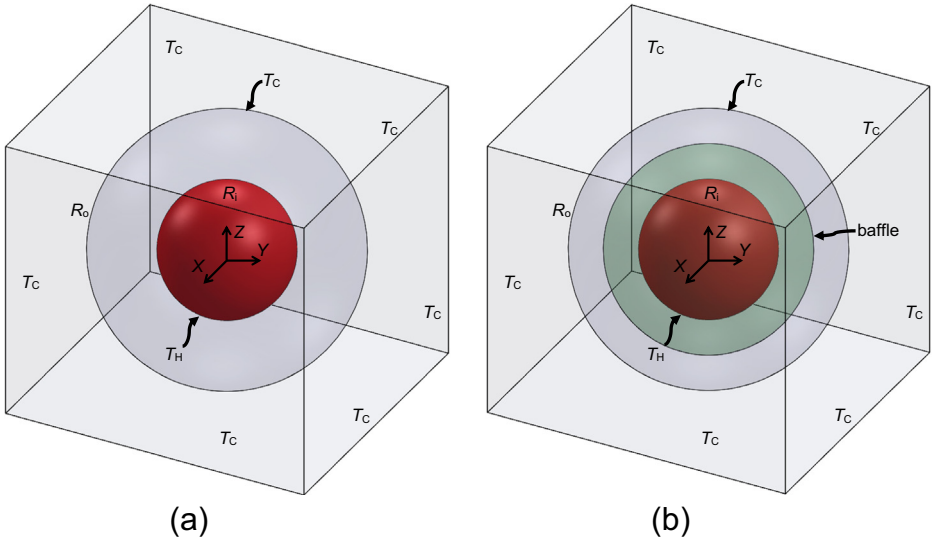

Fig. 1. Physical model and system of coordinates for the spherical shell: (a) with no internal baffles; (b) with a single internal baffle and two concentric equi-spaced layers.

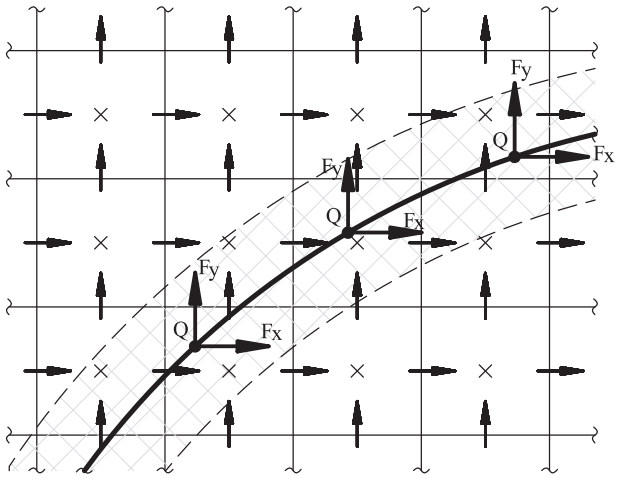

Fig. 2. A schematic of staggered grid discretization of a two-dimensional computational domain D with a segment of immersed boundary of a body B. A virtual shell, whose thickness is equal to the grid cell width, is shaded. The horizontal and vertical arrows $(\rightarrow,\uparrow)$ represent the discrete u_i and v_i velocity locations, respectively. Pressure p_j and temperature T_j are applied at the center of each cell $(\times)$. Lagrangian points $\xi_k(\xi_k,\eta_k)$ along ∂B are shown as black circles • where volumetric boundary forces $F_k=(F_x,F_y)$ $(\rightarrow,\uparrow)$ and volumetric boundary heat fluxes Q_k are applied.

arbitrary shape, B, within a computational domain, D (whose geometry does not, in general, have to conform to the underlying spatial grid), is represented by the surface, ∂B, determined by a set of Lagrangian points, $\boldsymbol{X}_k$. The same distance between neighboring points approximately equal to the grid size should be preserved to provide high accuracy [17].

We next associate a discrete volume ΔV_k with each Lagrangian point $\boldsymbol{X_k}$, such that an ensemble of these volumes forms a thin shell. The thickness of this virtual shell is equal to the width of the grid cell. At the Lagrangian points, appropriate volumetric forces, $\boldsymbol{F}_k$, and heat fluxes, Q_k, are applied to enforce the non-slip velocity and the Dirichlet temperature boundary conditions along ∂B. Since the location of the Lagrangian boundary points does not necessarily coincide with the underlying spatial discretization, regularization and interpolation operators must be defined to convey information about the immersed body in both directions. The regularization operator R smears volumetric forces, $\boldsymbol{F}_k$, and heat fluxes, Q_k, on the nearby computational domain, while the interpolation operator I acts in the opposite direction and imposes non-slip/thermal boundary conditions on the points located on the body surface:

$$R(\boldsymbol{F}_k(\boldsymbol{X}_k),Q_k(\boldsymbol{X}_k))=\int_S(\boldsymbol{F}_k(\boldsymbol{X}_k),Q_k(\boldsymbol{X}_k))\cdot\delta(\boldsymbol{x}_i-\boldsymbol{X}_k)dV_{Sk} \tag{4}$$

$$I(\boldsymbol{u}(\boldsymbol{x}_i),\theta(\boldsymbol{x}_i))=\int_\Omega(\boldsymbol{u}(\boldsymbol{x}_i),\theta(\boldsymbol{x}_i))\cdot\delta(\boldsymbol{X}_k-\boldsymbol{x}_i)\mathrm{dV}_{\Omega i}, \tag{5}$$

where S corresponds to all cells belonging to the immersed body surface, Ω corresponds to a group of the flow domain cells located in the close vicinity to the immersed body surface, dV_{Sk} corresponds to the infinitesimal volume surrounding each Lagrangian point k, and $\mathrm{dV}_{\Omega i}$ is the volume of the corresponding cell of the flow domain, whose velocity and temperature values are explicitly involved in enforcing boundary conditions at point k of the immersed body. Note that in the present formulation $\mathrm{dV}_{Sk}\approx\mathrm{dV}_{\Omega i}$. Convolutions with the Dirac delta function δ are used to facilitate the exchange of information to and from ∂B. Among the variety of discrete delta functions available, the function described by Roma et al. [18], specifically designed for use on staggered grids, where even/odd de-coupling does not occur, was chosen:

$$d(r)=\begin{cases}\frac{1}{6\Delta r}\left[5-3\frac{|r|}{\Delta r}-\sqrt{-3\left(1-\frac{|r|}{\Delta r}\right)^2+1}\right] & \text{for } 0.5\Delta r\leqslant|r|\leqslant1.5\Delta r,\\ \frac{1}{3\Delta r}\left[1+\sqrt{-3\left(\frac{|r|}{\Delta r}\right)^2+1}\right] & \text{for } |r|\leqslant0.5\Delta r,\\ 0 & \text{otherwise.}\end{cases} \tag{6}$$

The discrete delta function, $d(r)$, is supported over only three cells, which comprises an advantage for computational efficiency. The discrete forms of the regularization (4) and interpolation (5) operators for $3D$ geometry are governed by Eqs. (7) and (8) respectively:

$$(\boldsymbol{f}_i,q_i)=\Delta x^3\sum_k(\boldsymbol{F}_k,Q_k)d(\epsilon_k-x_i)d(\eta_k-y_i)d(\zeta_k-z_i) \tag{7}$$

$$(\boldsymbol{U}_k,\Theta_k)=\Delta x^3\sum_i(\boldsymbol{u}_k,\theta_k)d(x_i-\epsilon_k)d(y_i-\eta_k)d(z_i-\zeta_k), \tag{8}$$

where $\boldsymbol{f}_i,q_i$ are the discrete volumetric force and heat source defined on the staggered grid (x_i,y_i,z_i) and $\boldsymbol{U}_k,\Theta_k$ are the discrete boundary velocity and temperature defined at k-th Lagrangian point (ϵ,η,ζ).

Among the vast variety of existing pressure–velocity segregated solvers, the code recently developed and parallelized by Vitoshkin and Gelfgat [19] was chosen. The solver implements an algorithm based on the tensor product factorization (TPF) method combined with the Thomas solver (TPT), comprising an essentially direct method for the inversion of Helmholtz operators in discretized NS and energy equations. It was shown by Vitoshkin and Gelfgat [19] that the developed approach is about 10 times faster than the commonly used BICG algorithm when tested for the simulation of natural convection in cube on a 100^3 grid and the range of $10^5\leqslant Ra\leqslant10^7$. In an attempt to preserve the high efficiency of the solver, the current study implemented a direct forcing approach, which was introduced by Mohd-Yusof and coauthors [20,21] with an explicit formulation of forces and heat fluxes applied at Lagrangian points. In this way, the structure of discrete operators formulated in [19] was not affected, thus preserving the high efficiency of the original algorithm. The direct forcing method approximates the boundary force for rigid bodies with an intermediate non-solenoidal velocity field $\boldsymbol{u}^*$ initially calculated by ignoring the presence of the immersed body. Next, the Lagrangian force is implemented directly into the momentum equation by substituting the regularized no-slip condition near the immersed boundary:

$$\boldsymbol{F}^*(\boldsymbol{X}_k,t^n)=\frac{\boldsymbol{U}^\Gamma(\boldsymbol{X}_k,t^n)-\boldsymbol{U}^*(\boldsymbol{X}_k,t^n)}{\Delta t}, \tag{9}$$

where $\boldsymbol{U}^*$ represents the values of the boundary velocity obtained by interpolation of the nearby non-solenoidal (predicted) velocity field on the immersed body surface, and $\boldsymbol{U}^\Gamma$ corresponds to the preset boundary velocity (which is zero for the stationary boundary). In the next step, the volumetric boundary forces, $\boldsymbol{F}_k^*$, implemented at Lagrangian points, are regularized (smeared) over the adjacent volumes of the computational domain by Eq. 7 and contribute as sources to the corresponding NS equations:

$$\frac{\boldsymbol{u}^*-\boldsymbol{u}^n}{\Delta t}+(\boldsymbol{u}^n\cdot\nabla)\boldsymbol{u}^n-\boldsymbol{f}^*=-\nabla p^{n+1}+\sqrt{\frac{Pr}{Ra}}\nabla^2\boldsymbol{u}^*+\theta^n\overrightarrow{e_z}. \tag{10}$$

Finally, the algorithm completes the time step with the usual solution of the pressure Poisson equation and the consequent projection

step [22]. Similar to the velocity correction procedure, the preset immersed boundary temperatures Θ^{Γ} are enforced by solving the following heat transfer equation:

$$Q^*(\boldsymbol{X}_k, t^n) = \frac{\boldsymbol{\Theta}^{\Gamma}(\boldsymbol{X}_k, t^n) - \boldsymbol{\Theta}^*(\boldsymbol{X}_k, t^n)}{\Delta t}, \tag{11}$$

where the temperature of the Lagrangian points Θ^* is an interpolation of the intermediate temperature field θ^* initially computed by ignoring the presence of the immersed body and Q^* is a non-dimensional volumetric heat source/sink, whose value, regularized (smeared) by Eq. 7 enters as a source into the corresponding energy equations:

$$\frac{\boldsymbol{\theta}^* - \boldsymbol{\theta}^n}{\Delta t} + (\boldsymbol{u}^n \cdot \nabla)\boldsymbol{\theta}^n - q^* = \frac{1}{\sqrt{PrRa}} \nabla^2 \theta^{n+1}. \tag{12}$$

It should be emphasized that the source/sink q^* value is relevant only if the preset Dirichlet/Neumann boundary conditions have to be enforced (i.e., in the presence of a thermally active immersed surface). If the immersed body is exposed only to convective flow and does not actively emit/absorb the heat by itself, then only non-slip boundary conditions are enforced on the immersed surface. In this case, a zero value is assigned to the q^* term appearing in Eq. (12). Formally, this imposes zero thermal resistance in the direction normal to the body surface, in accordance with the assumptions typically treating the internal baffle as an idealized zero thickness surface. Note also that, due to the stationary boundaries, the interpolation/regularization operators can be pre-computed for each prescribed immersed surface: there is no need to employ a delta function at each time step, since it will yield the same result, thereby considerably decreasing the computational effort.

The direct forcing approach has two major drawbacks. First, it explicitly enforces the no-slip condition on $\boldsymbol{u}^*$ but not on $\boldsymbol{u}^{(n+1)}$. A projection step is therefore later applied to project the intermediate velocity, $\boldsymbol{u}^*$, onto the solenoidal solution space. Second, although the problem discussed is elliptic, the Lagrangian volumetric forces $\boldsymbol{F}^*$ and heat sources Q^* are calculated locally at every k-th point of the immersed body, without taking into account their mutual interaction at a given time step. Over the recent years a number of approaches have been developed to remedy the limitations of the direct forcing approach. Taira and Colonius [17] proposed an implicit treatment of both the pressure and boundary force as a single set of Lagrange multipliers in the modified Poisson equation. Ren et al. [23,24] implicitly evaluate all the boundary forces and heat sources by treating them as unknowns of a single system of equations. Another approach is to introduce an iterative procedure for Euler–Lagrange coupling which yields a substantially better imposition of boundary conditions at the interface [25,26]. Unfortunately, none of the above approaches can be efficiently utilized in numerical simulations of the presently discussed flow. The first approach requires a substantial modification of the existing numerical time stepper, the second approach is prohibitively expensive for the realistic 3D configurations and the third one locally deteriorates the momentum and the thermal balances, which in the case of large *Re* or *Ra* numbers can significantly affect velocity and temperature fields close to the immersed boundaries. For this reasons all the above modifications of the original direct forcing approach [20,21] were not used in the present study and correct imposition of boundary conditions was achieved by utilizing small time step, which was equal $\Delta t = 10^{-4}$ for all the simulations performed. It was also verified that a further decrease of the time step to $\Delta t = 10^{-5}$ does not result in any significant changes in the obtained solutions. Eqs. (9) and (11) imply utilizing a first order accuracy finite difference scheme for the time disretization. As a result the original time stepper [19], in which the time derivative in the unsteady momentum and energy equations are approximated by a second order backward differentiation, was modified. At the same time we utilized the original discretization of all the spatial terms in the NS Eqs. (1)–(3) implemented by the second order finite volume method [27]. Next we define the Nusselt number *Nu* as a ratio of convective to conductive fluxes. Utilizing the same scaling as in Eqs. (1)–(3), the non-dimensional heat flux from the infinitesimal immersed surface is defined as:

$$\frac{\partial \Theta^*}{\partial \hat{n}} = \Delta x \sqrt{PrRa} Q^* \tag{13}$$

where Q^* is defined in Eq. (11). The heat flux values averaged over the entire surface are then used for calculation of the *Nu* numbers at the inner Nu_i and outer Nu_o boundaries of the spherical shell:

$$Nu_i = \frac{1}{\pi D_i D_o}\left(\overline{\frac{\partial \Theta^*}{\partial \hat{n}}}\right) A_i, Nu_o = \frac{1}{\pi D_i D_o}\left(\overline{\frac{\partial \Theta^*}{\partial \hat{n}}}\right) A_o \tag{14}$$

3. Verification study

3.1. Natural convection in a cubic enclosure with a sphere.

The developed solver was first verified by simulating the natural convection flow developing in the presence of isothermal hot sphere placed within a cubic container with all isothermal cold walls. The flow is governed by the same non-dimensional NS Eqs. (1)–(3) as the original problem with the only difference that all the length scales are normalized by the cube side length, *d*. The inner hot sphere is located on the vertical centerline of the cube and its distance to the cube center is determined by the non-dimensional parameter $-0.25 \leqslant \delta \leq 0.25$, defined as $\delta = Z_c - Z_{sph}$, where Z_c and Z_{sph} are the non-dimensional Z coordinates corresponding to the centers of the cubic container and of the sphere, respectively [28]. All the results were obtained on a 200^3 uniform grid. Fig. 3 shows the flow characteristics in terms of the temperature distribution and projection of the path lines on a mid-plane cross section obtained for the $Ra = 10^4, 10^5, 10^6$ and $\delta = -0.25, 0, 0.25$ values. There is an excellent agreement between the characteristics of the presently computed flow and the previously published results [28] for the entire range of *Ra* and δ values. For all the *Ra* values the flow at $\delta = -0.25$ is characterized by a clearly distinguished thermal plume rising up from the top of the sphere. The plume becomes less developed as δ increases and the restricting effect of the top boundary on the rising up convective flow becomes more pronounced. All the configurations are characterized by the strong temperature gradients just below the sphere and close to the cube top boundary, indicting existence of thin boundary layers in these regions. When $\delta = 0.25$ the thermal plume, localized at the top half of the cube, is radially squeezed for all the *Ra* values, giving rise to development of thermally stratified region with almost zero velocities below the sphere. Spiral form of the flow path lines observed for all the configurations presented in Fig. 3 clearly indicate the 3D character of the flow which is a consequence of the end-wall effects.

Table 1 compares between the presently obtained an the previously published [28] values of average *Nu* numbers. An acceptable agreement between the results is observed for the entire range of *Ra* numbers. The differences between the results grow up with increasing the *Ra* values which can apparently be a consequence of different approaches utilized for calculation of the *Nu* numbers.

3.2. Natural convection in the spherical annuli – axi-symmetric flow

The results obtained for the flow inside spherical annuli were also successfully verified by comparison with numerical data

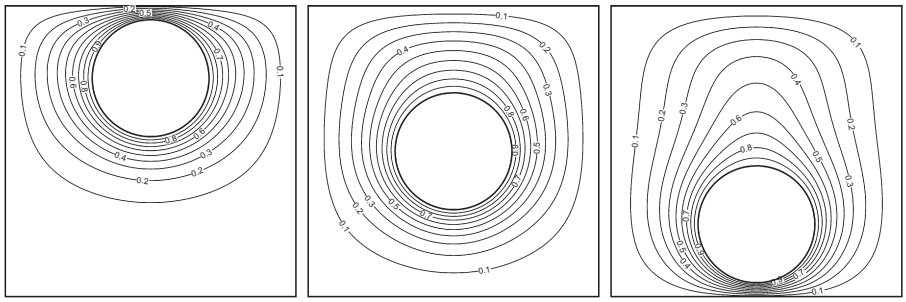

(a) Temperature distribution of the mid-plane cross section, $Ra = 10^4$

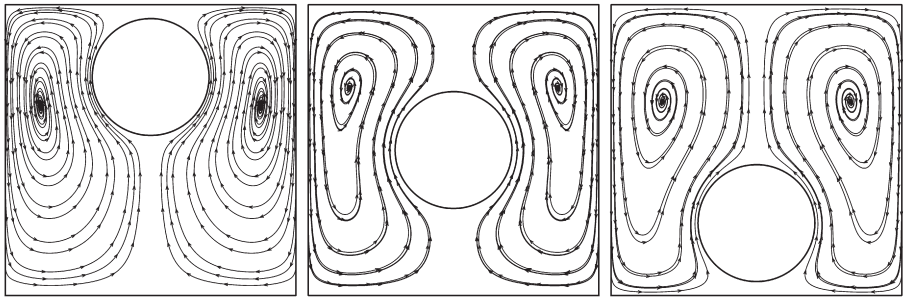

(b) Path lines projection on the mid-plane cross section, $Ra = 10^4$

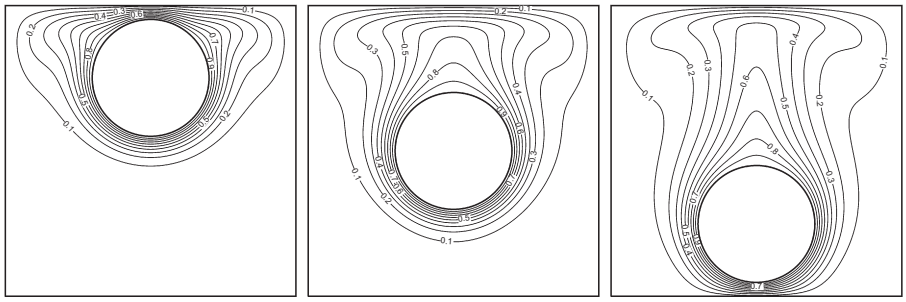

(c) Temperature distribution of the mid-plane cross section, $Ra = 10^5$

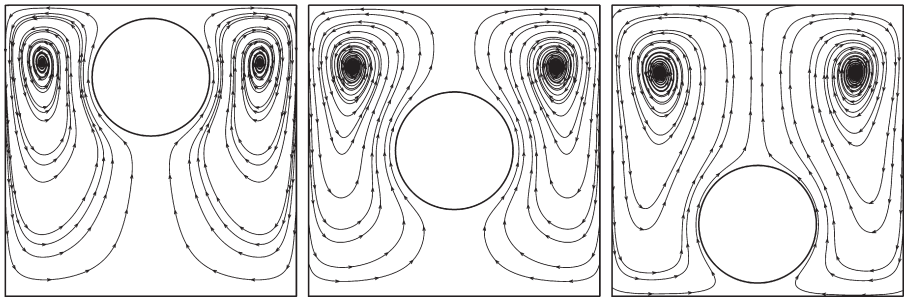

(d) Path lines projection on the mid-plane cross section, $Ra = 10^5$

Fig. 3. Flow characteristics on a mid-plane cross section as a function of *Ra* number: temperature distribution and path lines projection obtained for the values of $\delta = -0.25; 0; 0.25$ on a 200^3 grid.

available in the literature. Fig. 4 presents a comparison between the axi-symmetric temperature fields provided by [29] for three different *Ra* numbers and the corresponding results obtained in this study by fully three-dimensional simulations. There is a good qualitative and quantitative agreement between the corresponding temperature fields for the whole range of *Ra* numbers. Typical of steady laminar flows in spherical shells, the results obtained by the fully three-dimensional solver preserve the flow's axi-symmetry.

3.3. Grid independence study

To perform a grid independence study the natural convection flow was simulated inside a double-walled spherical shell (without internal baffles) on 200^3 and 300^3 uniform grids for $Ra = 10^3, 10^4, 10^5$. The results of all the velocity components and temperature were collected from the control points located on the spherical shell center-lines. For both grids the flow characteristics were acquired at eight control points uniformly distributed

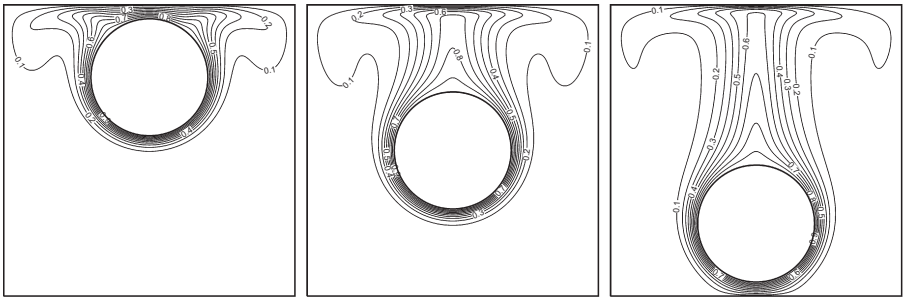

(e) Temperature distribution of the mid-plane cross section, $Ra = 10^6$

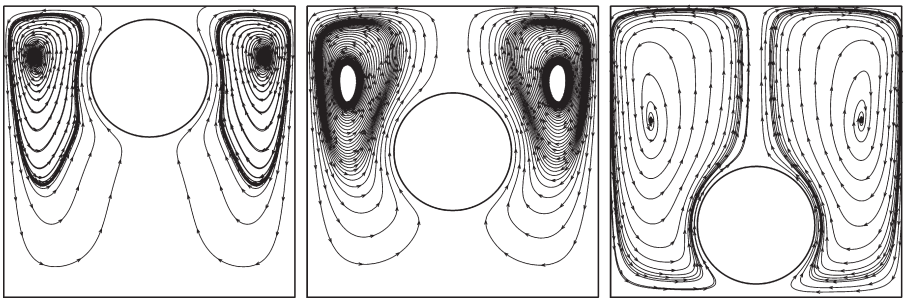

(f) Path lines projection on the mid-plane cross section, $Ra = 10^6$

Fig. 3 (*continued*)

Table 1
Comparison between the present and the scanned [28] average *Nu* values obtained for the flow developing in the presence of isothermal hot sphere placed within a cubic container with all isothermal cold walls.

δ	$Ra = 10^4$		$Ra = 10^5$		$Ra = 10^6$	
	Ref. [28]	Present	Ref. [28]	Present	Ref. [28]	Present
−0.25	9.867	10.199	13.665	13.774	20.890	21.993
−0.2	8.843	9.117	12.931	13.058	20.631	21.862
−0.1	8.087	8.451	12.729	13.105	20.772	22.164
0	7.859	8.314	12.658	13.415	20.701	22.344
0.1	7.947	8.507	12.351	13.446	20.367	22.525
0.2	8.615	9.266	12.254	13.635	19.664	22.208
0.25	9.621	10.387	12.944	14.426	19.721	22.393

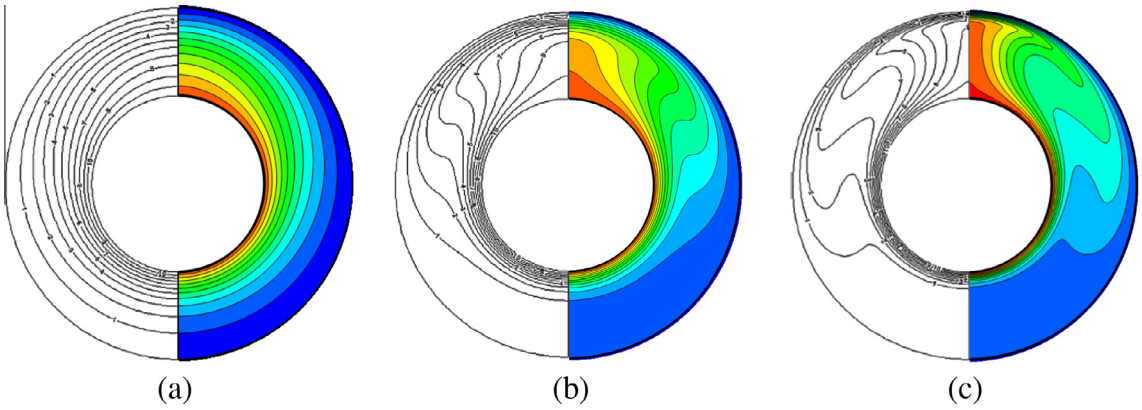

Fig. 4. Comparison between the axi-symmetric temperature field provided by Dehghan and Masih [29] and the present results obtained by fully three-dimensional simulations for: (a) $Ra = 10^3$; (b) $Ra = 10^4$; (c) $Ra = 10^5$. The contour colors correspond to 10 equi-spaced values of temperature in the range of $0 < \theta < 1$.(For interpretation of the references to colour in this figure legend, the reader is referred to the web version of this article.)

along each centerline (four from each side of the center of spherical shell), as presented in Table 2. Most of the results obtained on the two grids are in excellent agreement. A deviation between the corresponding fields appears in the third decimal digit, as expected for the second order accuracy method. For all the cases the axi-symmetry of the steady flow is clearly recognized by verifying

Table 2
Flow characteristics along the spherical shell center-lines, all the velocity components (u_x, u_y, u_z) are multiplied by a factor of 10^3.

$Ra = 10^3, Y = Z = 0, u_y = 0$							$Ra = 10^4, Y = Z = 0, u_y = 0$						$Ra = 10^5, Y = Z = 0, u_y = 0$					
	200^3 grid			300^3 grid			200^3 grid			300^3 grid			200^3 grid			300^3 grid		
X	u_x	u_z	θ	u_x	u_z	θ	u_x	u_z	θ	u_x	u_z	θ	u_x	u_z	θ	u_x	u_z	θ
−1.8	7.222	−187.2	0.1005	7.667	−187.6	0.1002	28.66	−244.3	0.1049	29.49	−241.3	0.1029	16.96	−239.2	0.1740	17.90	−234.3	0.1729
−1.6	17.17	−119.7	0.2242	17.82	−119.4	0.2225	70.59	−161.7	0.1771	71.36	−160.7	0.1733	11.77	−5.502	0.1922	11.73	−5.251	0.1873
−1.4	15.22	110.2	0.3833	15.75	110.5	0.3802	73.28	69.30	0.2065	74.19	65.90	0.2022	14.81	70.80	0.1580	16.32	70.74	0.1513
−1.2	3.893	306.7	0.6272	4.087	309.5	0.6228	34.84	431.1	0.3731	35.74	426.2	0.3652	28.21	223.0	0.1892	29.39	211.1	0.1789
1.2	−3.895	306.7	0.6272	4.087	309.5	0.6228	−34.84	431.0	0.3730	−35.74	426.2	0.3652	−28.20	223.0	0.1891	−29.39	211.2	0.1789
1.4	−15.22	110.2	0.3832	−15.76	110.5	0.3802	−73.28	69.30	0.2065	−74.19	65.90	0.2022	−14.81	70.73	0.1580	−16.32	70.72	0.1513
1.6	−17.17	−119.7	0.2242	−17.83	−119.4	0.2225	−70.59	−161.7	0.1771	−71.36	−160.7	0.1733	−11.78	−5.552	0.1921	−11.73	−5.226	0.1873
1.8	−7.221	−187.2	0.1005	−7.667	−187.6	0.1002	−28.66	−244.3	0.1049	−29.49	−241.3	0.1029	−16.96	−239.4	0.1740	−17.90	−234.3	0.1729

$Ra = 10^3, X = Z = 0, u_x = 0$							$Ra = 10^4, X = Z = 0, u_x = 0$						$Ra = 10^5, X = Z = 0, u_x = 0$					
	200^3 grid			300^3 grid			200^3 grid			300^3 grid			200^3 grid			300^3 grid		
Y	u_y	u_z	θ	u_y	u_z	θ	u_y	u_z	θ	u_y	u_z	θ	u_y	u_z	θ	u_y	u_z	θ
−1.8	7.222	−187.2	0.1005	7.668	−187.6	0.1002	28.66	−244.3	0.1049	29.49	−241.3	0.1029	16.97	−239.4	0.1740	17.90	−234.3	0.1729
−1.6	17.17	−119.7	0.2242	17.82	−119.4	0.2225	70.58	−161.7	0.1771	71.36	−160.7	0.1733	11.78	−5.533	0.1922	11.73	−5.234	0.1873
−1.4	15.22	110.2	0.3833	15.75	110.5	0.3802	73.27	69.35	0.2065	74.18	65.90	0.2022	14.80	70.80	0.1580	16.32	70.75	0.1513
−1.2	3.894	306.7	0.6272	4.088	309.5	0.6228	34.82	431.1	0.3731	35.74	426.2	0.3652	28.18	223.1	0.1892	29.39	211.2	0.1789
1.2	−3.894	306.7	0.6272	−4.088	309.5	0.6228	−34.82	431.0	0.3730	−35.74	426.2	0.3652	−28.21	223.0	0.1891	−29.40	211.1	0.1789
1.4	−15.22	110.2	0.3832	−15.76	110.4	0.3802	−73.28	69.33	0.2065	−74.19	65.86	0.2022	−14.81	70.86	0.1580	−16.32	70.73	0.1513
1.6	−17.17	−119.7	0.2242	−17.83	−119.4	0.2225	−70.59	−161.7	0.1771	−71.36	−160.7	0.1733	−11.78	−5.461	0.1922	−11.74	−5.238	0.1873
1.8	−7.221	−187.2	0.1005	−7.666	−187.6	0.1002	−28.66	−244.3	0.1049	−29.49	−241.3	0.1029	−16.96	−239.4	0.1740	−17.90	−234.3	0.1729

$Ra = 10^3, X = Y = 0, u_x, u_y = 0$					$Ra = 10^4, X = Y = 0, u_x, u_y = 0$				$Ra = 10^5, X = Y = 0, u_x, u_y = 0$			
	200^3 grid		300^3 grid		200^3 grid		300^3 grid		200^3 grid		300^3 grid	
Z	u_z	θ	u_z	θ	u_z	θ	u_z	θ	u_z	θ	u_z	θ
−1.8	16.86	0.0524	17.97	0.0516	9.253	0.0085	10.19	0.0079	−1.418	0.0019	0.151	0.0014
−1.6	55.71	0.1271	56.86	0.1248	39.06	0.0216	39.82	0.0205	7.026	0.0045	9.324	0.0035
−1.4	86.25	0.2564	87.36	0.2526	79.05	0.0554	79.30	0.0535	28.54	0.0100	30.59	0.0082
−1.2	63.46	0.5216	64.99	0.5154	87.50	0.2298	88.17	0.2237	59.96	0.0552	60.56	0.0506
1.2	69.87	0.8508	71.39	0.8527	94.46	0.9346	93.41	0.9334	173.8	0.9439	172.0	0.9444
1.4	133.8	0.7085	136.2	0.7134	195.1	0.8938	193.4	0.8921	363.1	0.9116	363.2	0.9125
1.6	120.3	0.5183	123.9	0.5256	217.7	0.8590	217.2	0.8570	402.9	0.8880	404.9	0.8891
1.8	47.62	0.2591	50.75	0.2659	129.2	0.6856	132.0	0.6904	264.8	0.8688	266.7	0.8699

the same values of the flow fields in the reflection symmetry points on the X and Y centerlines. Note also that zero ($o(10^{-6})$) values of velocity components in transverse direction were obtained for all the cases, additionally verifying an axi-symmetry of the obtained steady flow. Basing on the performed grid independence analysis all the results of the present study were further calculated on the 200^3 uniform grid.

3.4. Verification of the average Nu values

Precise estimation of the average Nu number comprises an essential criterion for verification of any numerical solver and is particulary critical for the IBM. The IBM relies on a uniform Cartesian grid, which does not allow further local, stretching for a more precise resolution of the thinnest boundary layers. In this case, a more precise estimation of the Nu values is achieved by utilizing the law of conservation of heat flux (see Eq. (13)) rather than simply calculating the near-surface temperature gradient. A comparison between the available and our estimated Nu values for various spherical shell configurations and different Ra numbers corresponding to steady-state flow is summarized in Table 3. It is remarkable that for steady state flow acceptable agreement in Nu values is observed for the fully three-dimensional and axi-symmetric simulations. The picture is, however, quite different for unsteady non-axi-symmetric flows, which (for the same operating conditions) are characterized by an enhanced heat flux compared to the corresponding axi-symmetric idealizations (see Table 4). At the same time, there is good agreement for all the Nu when compared with the recent results of Feldman and Colonius [15]– all obtained by a three-dimensional analysis. In all cases, the same Nu values (up to the third decimal digit) were obtained for the external and internal shell boundaries by their time and space averaging, after an asymptotic quasi-state solution was reached. This finding verifies the heat flux conservation over the entire computational domain. Note also an excellent agreement between the Nu values obtained on 200^3 and on 300^3 grids which can be seen as additional justification of the grid independence of the obtained results.

4. Results and discussion

The IBM enables efficient manipulation of the orientation of the internal layers of the spherical shell so as to achieve optimized thermal insulation. Among the large number of possibilities, the present study focusses on an investigation of equi-spaced/non-equi-spaced concentric and horizontally/vertically eccentric orientations of the internal layers. All the numerical simulations were performed for a spherical shell characterized by $\phi = D_i/Do = 0.5$ on a 200^3 uniform grid.

4.1. Concentric equi-spaced internal layers

As the first step, the natural convection flow inside a spherical shell with up to four concentric equi-spaced internal layers was investigated. Following the recent works of Samanta et al. [13], Feldman et al. [14], and Feldman and Colonius [15], zero wall thickness was assumed for all the internal baffles, providing zero thermal resistance in the radial direction. In addition, non-slip boundary conditions for all the velocity components were imposed on all internal baffles and external boundaries of the shell. Typical steady state temperature distributions along with the flow path lines obtained in a mid cross-section of the spherical shells with up to four equi-spaced internal layers for moderate, $Ra = 10^4$, and high, $Ra = 5 \times 10^5$, Rayleigh numbers are shown in Figs. 5 and 6, respectively.

As expected, the steady flow obtained for all the configurations is axi-symmetric as can be verified by a concentric shape of the flow path lines characterizing toroidal convection cells occupying each layer. It was also found that the internal baffles embedded in the spherical shell have a pronounced effect on the redistribution of convective flow inside the shell as follows. First, the internal baffles stabilize the convective flow, thereby preserving steady-state regimes at much higher Ra values than those determining an instability onset in single-layered spherical shells. In fact, modified kidney shaped eddy pattern typical of high Ra values and wide shells and observed in Fig. 6a transforms into a crescent eddy pattern for the configurations containing internal baffles (see Figs. 14b–d). Second, the internal baffles suppress the convective component of the heat flux. As a result, a hot thermal plume rising up from the top of internal sphere either disappears at $Ra = 10^4$ or significantly weakens at $Ra = 5 \times 10^5$. The more internal baffles embedded the weaker the convective heat transfer and the closer the temperature distribution to that typical of a pure conduction regime. This observation is not surprising, since actual heat flux depends on the effective length scale which is a function of a number of internal baffles. We can then define an effective (modified) Ra^* number based on the distance between two adjacent baffles, which for the equi-spaced multi-layered spherical shell can be expressed as:

$$Ra^* = Ra/(N-1)^3, \tag{15}$$

where N is the total number of the shell boundaries (internal and external). The quantitative differences in the observed flow regimes can be quantified by examining both the $Nu - Ra$ and the $Nu - Ra^*$ functionalities of each configuration. The same temperature difference between the hot and cold boundaries, $\Delta\theta$ was chosen to provide a common basis for comparison. Fig. 7-a presents the $Nu - Ra$ functionality for spherical shells with two to five walls,

Table 4
Average (in time and in space) Nu numbers for unsteady 3D flow. Results reported for axi-symmetric flow are given in parentheses.

ϕ	Ra	Present (200^3 grid)	Present (300^3 grid)	Ref. [15]	Ref. [30]	Ref. [29]
0.667	1.0×10^4	1.811	1.826	1.793	(1.073)	(1.07138)
	1.0×10^5	3.321	3.375	3.243	(1.917)	(1.89756)
0.833	1.0×10^4	1.620	1.713	1.6523	(1.001)	(1.0028)
	1.0×10^5	3.274	3.276	3.0678	(1.008)	(1.0100)

Table 3
Average (in space) Nu numbers for steady laminar axi-symmetric flow.

ϕ	Ra	Present (200^3 grid)	Present (300^3 grid)	Ref. [15]	Ref. [30]	Ref. [29]	Ref. [8]
0.5	1.0×10^3	1.126	1.120	1.104	1.0990	1.1310	1.1021
	1.0×10^4	1.993	1.987	1.9665	1.9730	1.9495	1.9110
	1.0×10^5	3.461	3.452	3.4012	3.4890	3.4648	3.3555
0.667	1.0×10^3	1.069	1.081	1.04825	1.001	1.00115	
0.833	1.0×10^3	1.061	1.053	1.011	1.0	1.0018	

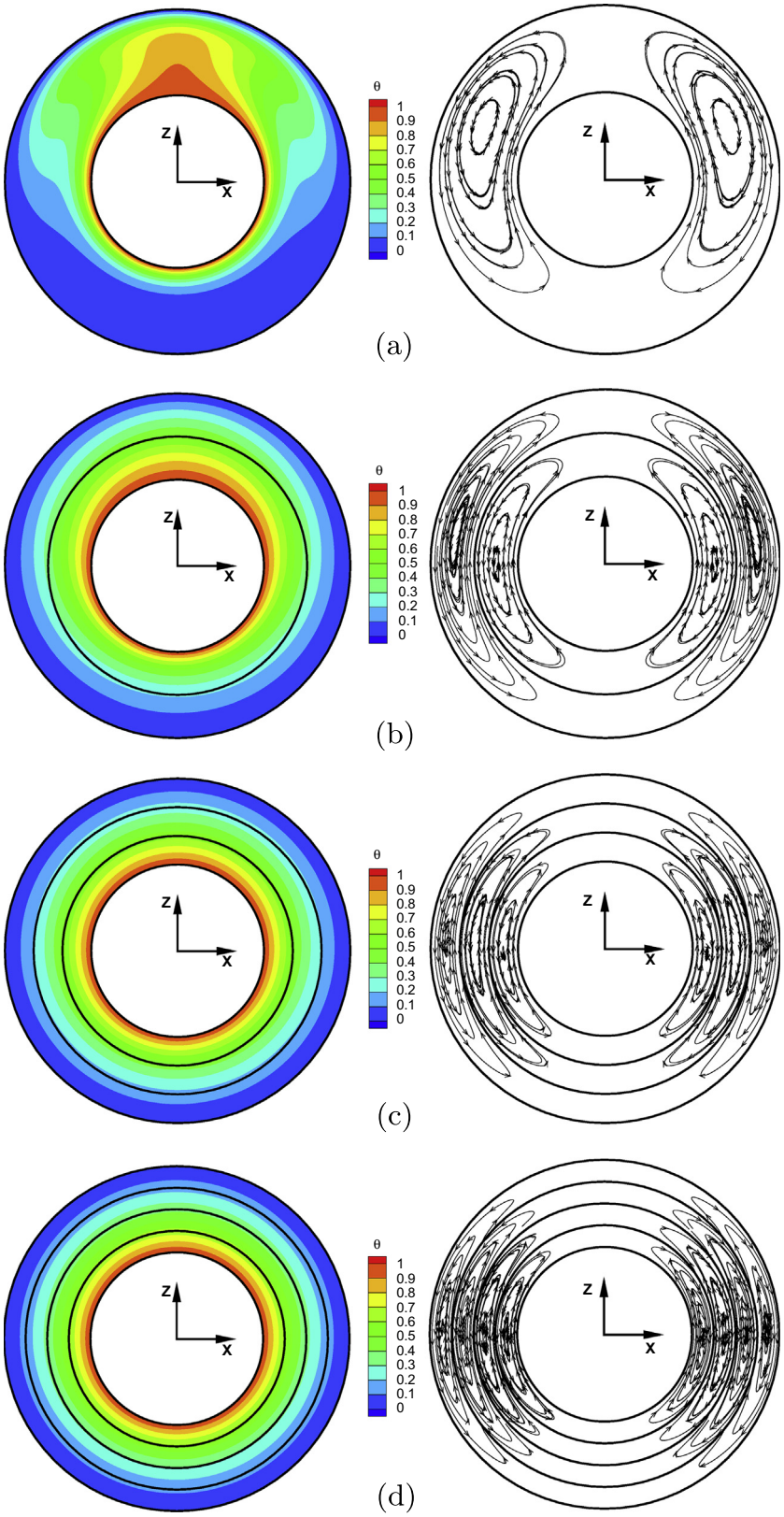

Fig. 5. Steady-state temperature distribution, θ, and projection of the flow path lines for $Ra = 10^4$ in the mid cross section of a spherical shell with: (a) one internal layer; (b) two equi-spaced internal layers; (c) three equi-spaced internal layers; (d) four equi-spaced internal layers.

when the *Ra* number is based on the total width *L*. In this case, the spherical shell is treated as a '*black box*' whose insulation efficiency is only estimated as a function of the number of equi-spaced concentric internal baffles. Four separate curves were obtained for the $Nu - Ra$ power law functionality, each corresponding to a different number of walls.

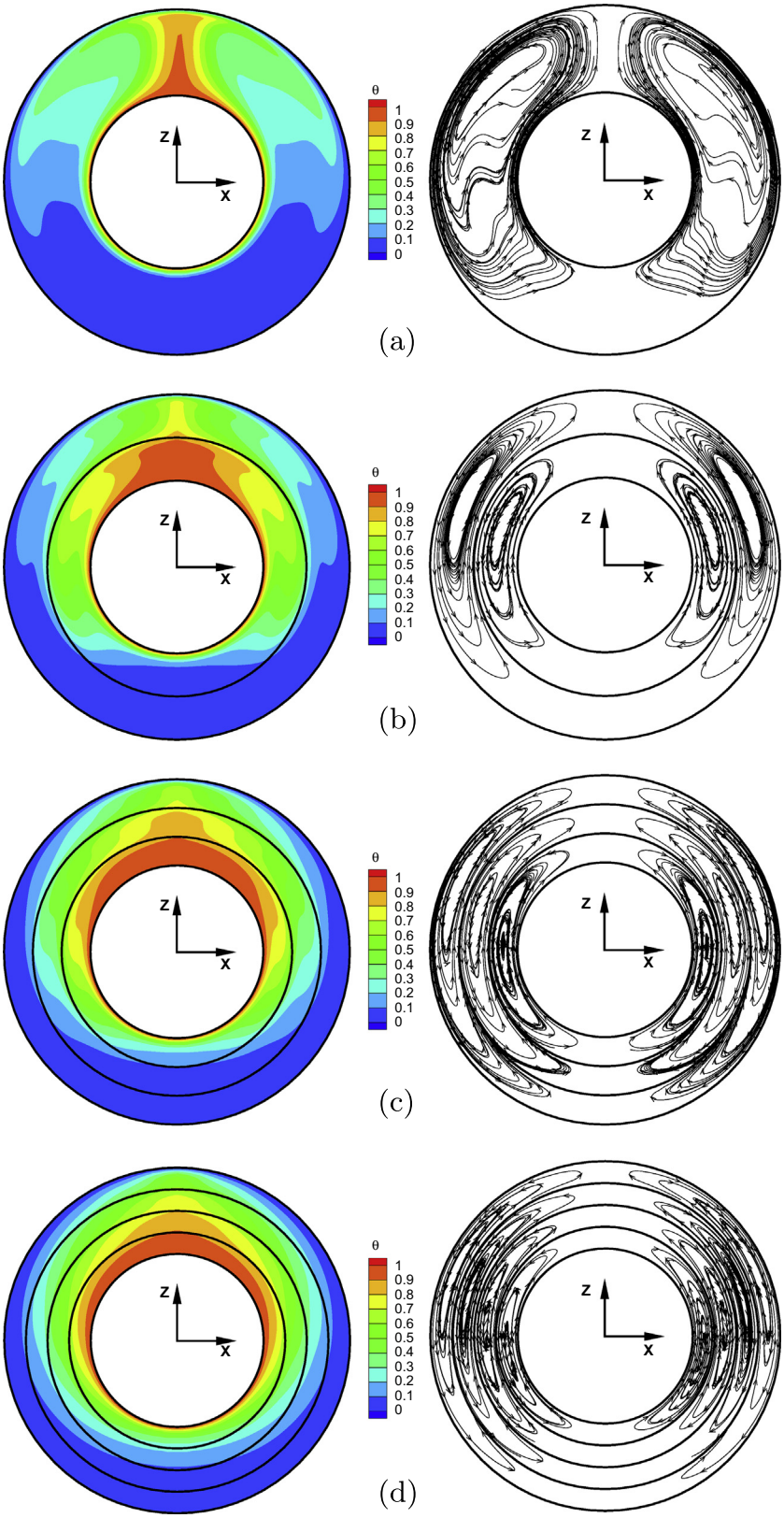

Fig. 6. Steady-state temperature distribution, θ, and projection of the flow path lines for $Ra = 5 \times 10^5$ in the mid cross section of a spherical shell with: (a) one internal layer; (b) two equi-spaced internal layers; (c) three equi-spaced internal layers; (d) four equi-spaced internal layers.

Note the good agreement between the current and the previously published results [4] obtained for a spherical shell without internal baffles for the entire range of *Ra* numbers. As expected, the insulation property of the spherical shell improves with the number of embedded baffles, leading to a considerable decrease in *Nu* for the same values of the *Ra* numbers. The maximal

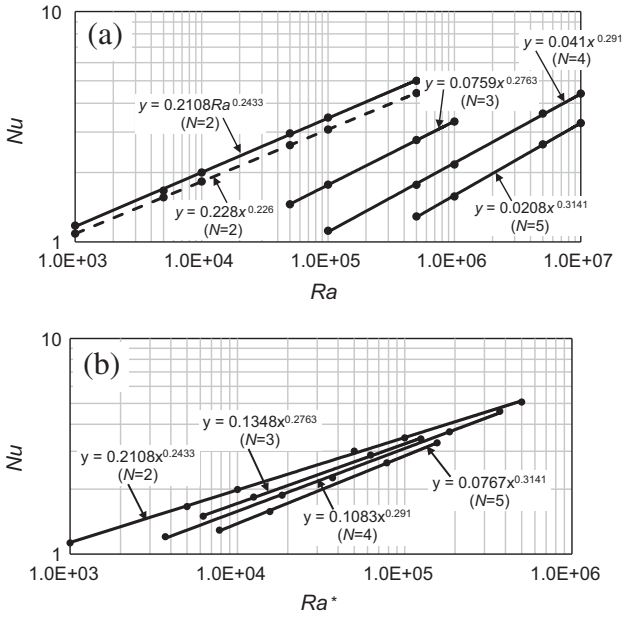

Fig. 7. Nu-Ra functionality obtained for spherical shells with different numbers of internal layers. The total number of walls for each spherical shell is given in parentheses. The dashed line corresponds to the universal correlation of Scanlan et al. [4] obtained for a single-layered spherical shell.

difference (up to four times) was observed at $Ra = 5 \times 10^5$ between the $N = 2$ and $N = 5$ configurations. To account for the effective length scale inherent to the multi-layered spherical shell the $Nu - Ra^*$ functionality, where Ra^* is the modified Rayleigh number defined in Eq. (15) is shown in Fig. 7-b. It can be seen that the curves corresponding to the different spherical shell configurations are now much closer clearly indicating that the effective length scale plays an important role in determining the overall heat flux through the shell boundaries. At the same time introducing the modified Ra^* number is not enough to obtain the $Nu - Ra^*$ functionality in a form of the single curve universally fitting all the configurations discussed. This is apparently due to the fact that the actual temperature difference between the adjacent baffles is much smaller then it was assumed. Looking for the ways to further generalize our analysis we examined the $Nu - Ra^*$ functionality for all the configurations discussed and recognized both a monotonic increase of the power law exponent and a monotonic decrease of the power law constant with an increasing number of layers. Formally denoting the power exponent by a and the power law constant by b, a functional relation of both quantities to the total number of shell boundaries, N was approximated by the least squares method:

$$a = 0.443N^{-1.064}, 2 \leqslant N \leqslant 5. \tag{16}$$

$$b = 0.202N^{0.270}, 2 \leqslant N \leqslant 5 \tag{17}$$

Next it would be a matter of straight algebra to derive a unified correlation based on the power law for the $Nu^* - Ra^*$ functionality for up to five walls (see Fig. 8):

$$Nu^* = Ra^{*0.32}, \tag{18}$$

where Nu^* is the modified Nu number defined as:

$$Nu^* = \left(\frac{Nu}{0.51N^{-1.21}}\right)^{1.65N^{-0.32}}, 2 \leqslant N \leq 5. \tag{19}$$

The equi-spaced concentric orientation of the internal layers is not the ultimate configuration to be considered for further

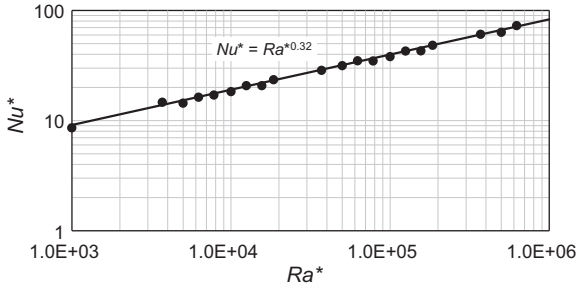

Fig. 8. $Nu^* - Ra^*$ functionality. The correlation for modified Nu^* is valid for multi-layered spherical shell containing up to five equi-spaced concentric walls (four internal layers).

improvement of the insulation efficiency of the spherical shell. In the following, three other configurations are discussed and their insulation properties are compared with the corresponding equi-spaced concentric.

4.2. Horizontally/vertically eccentric layers

A number of double-layered spherical shells with varying vertical and horizontal eccentricity values were investigated. The eccentricity, ϵ, is defined as:

$$\epsilon = |\mathbf{X}_{eccentric} - \mathbf{X}_{concentric}|/L, \tag{20}$$

where $\mathbf{X}_{eccentric}$ and $\mathbf{X}_{concentric}$ are the center coordinates of the eccentric internal baffle and concentric internal and external boundaries of the spherical shell, respectively. Fig. 9 presents the steady-state distribution of the temperature field, θ, and the projection of the flow path lines on the mid-plane cross section of a double-layered spherical shell for two different eccentricity values $\epsilon = 0.167, 0.335$, and $Ra = 5 \times 10^5$. The impact of the horizonal offset of the internal baffle is clearly reflected in the character of the thermal plume, which is biased to the side in the direction of the offset. Note that the eccentricity has a pronounced effect on the distribution of both the θ an the flow patterns in both layers. It is clear that the axial symmetry of the flow was broken and the flow is fully 3D. Non-negligible azimuthal velocities can be recognized by the presence of the flow path lines of a converging spiral shape in the center of some convection cells (see Fig. 9). Due to the lower temperature difference between the internal baffle and the external wall the thermal redistribution inside the second layer is affected to a lesser extent by the eccentricity of the internal wall – a trend that is apparently preserved with a further increase in the number of internal layers.

The influence of the offset of the internal wall along the vertical axis on the steady flow fields is demonstrated in Fig. 10. The flow obtained was simulated for the same parameters ($Ra = 5 \times 10^5$ and $\phi = 0.5$) and eccentricity values as in the previous case. It is remarkable that the high temperature region inherent in the configuration with the downward biased internal sphere is much narrower than that observed for spherical shell with the upward biased internal sphere. Thus, the distance between the top of the hot boundary and the internal baffle has a critical effect on the development of the thermal plume inside the layer adjacent to the hot boundary. The closer the internal wall to the top of the hot boundary, the less is the local effective length scale of the flow resulting in the lower velocity values of the thermal plume developed in that region. Similarly to the previously performed axi-symmetric simulations [8], a local increase of the distance between the internal baffle and the external boundary in the

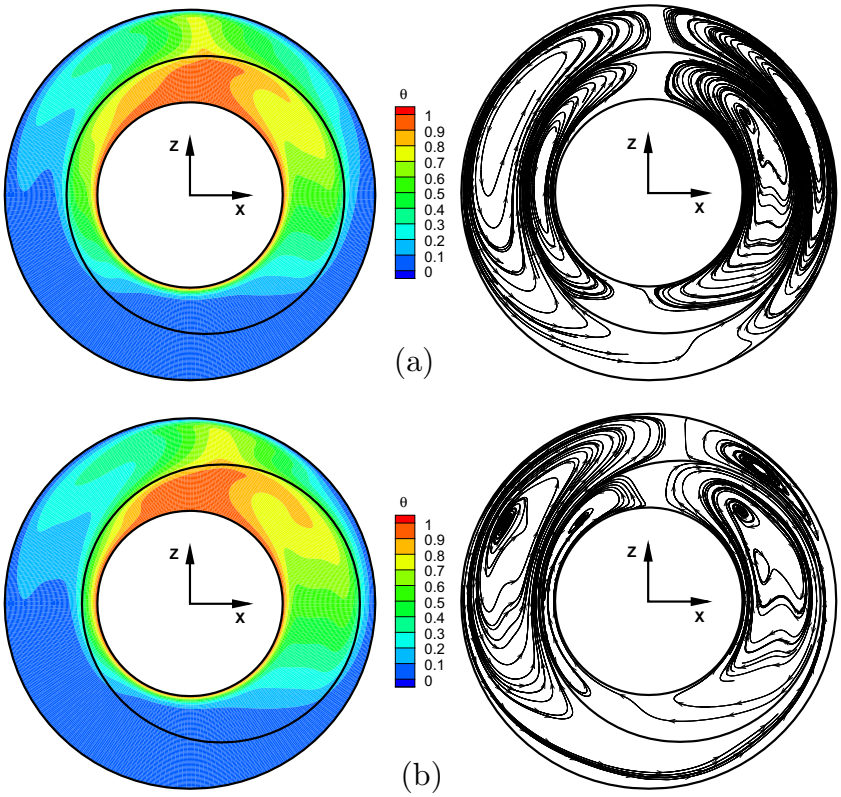

Fig. 9. Steady-state flow fields, obtained at the mid-plane cross section of a three-wall spherical shell for $Ra = 5 \times 10^5$. Contours of the temperature θ and projection of the flow path lines for: (a) $\epsilon = 0.167$; (b) $\epsilon = 0.335$.

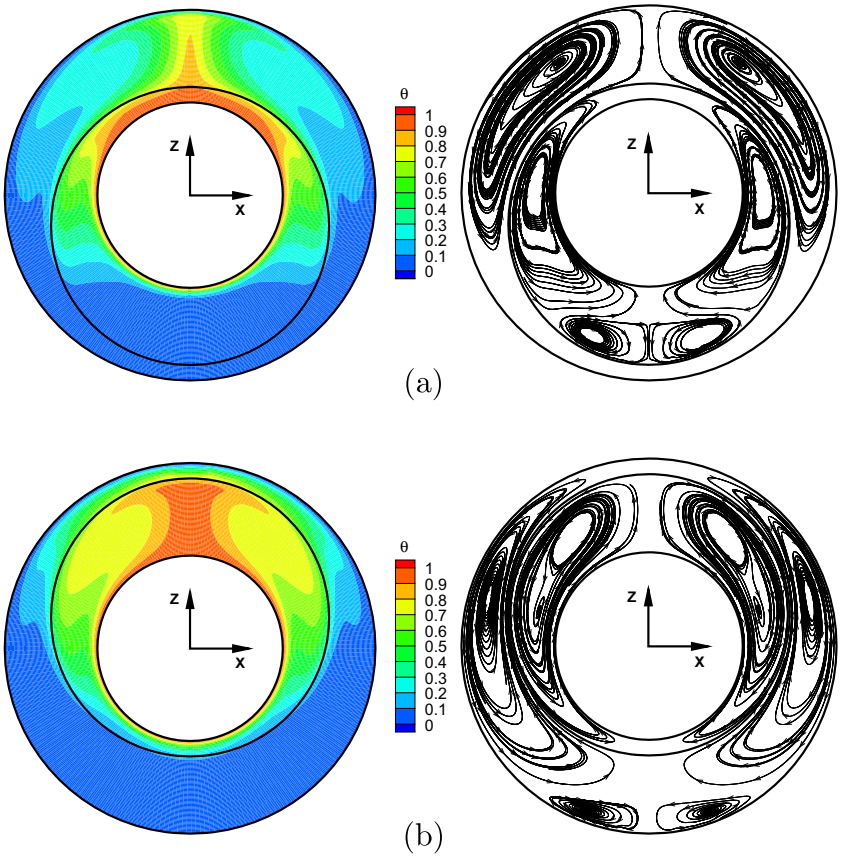

Fig. 10. Steady-state flow fields obtained at the mid-plane cross section of a three-wall spherical shell for $Ra = 5 \times 10^5$. Contours of the temperature θ and projection of the flow path lines for: (a) $\epsilon = 0.167$; (b) $\epsilon = 0.167$.

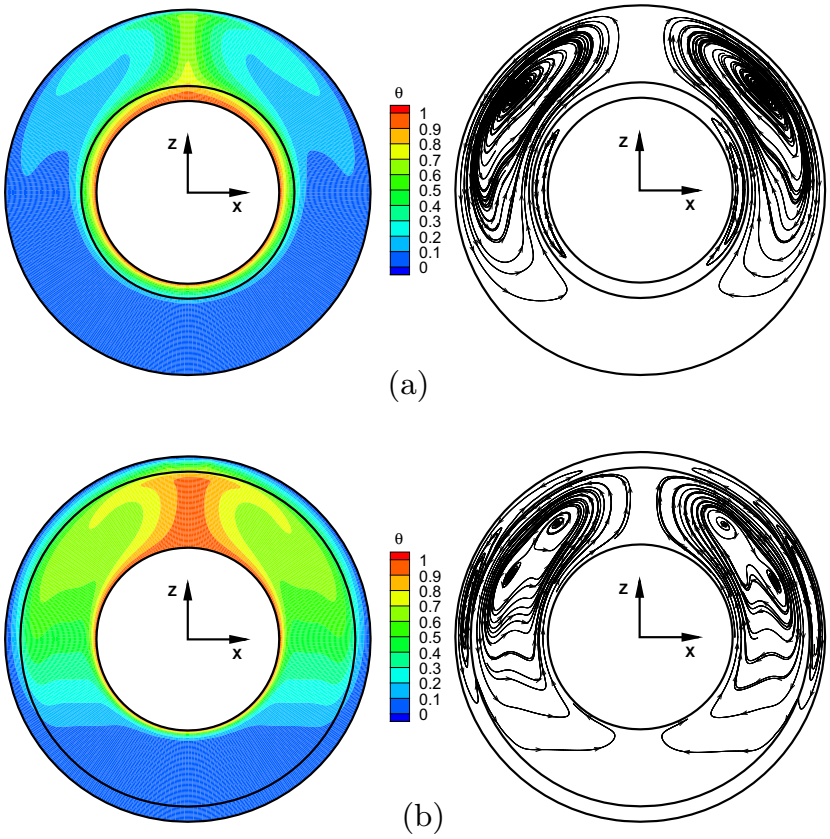

Fig. 11. Steady-state flow fields obtained at the mid cross section of a three-wall spherical shell for $Ra = 5 \times 10^5$. Contours of the temperature θ and projection of the flow path lines for: (a) $D_b/D_i = 1.17$; (b) $D_b/D_i = 1.83$.

bottom region gives rise to the multi-cell convection flow (see Fig. 10), not observed in either concentric configuration.

4.3. Non-equi-spaced concentric layers

We next focused on the investigation of the effect of a non-uniform width of the internal layers on the characteristics of the steady state flow developing inside the double-layered spherical shell. The non-uniform non-dimensional distance was defined in terms of the diameter ratio $1 \leqslant D_b/D_i \leq 2$, where, D_b corresponds to the diameter of internal baffle and D_i is the diameter of the hot boundary sphere. Note that the value $D_b/D_i = 1.5$ corresponds to the double-layered equi-spaced configuration. The numerical simulations were performed for two configurations corresponding to $D_b/D_i = 1.17, 1.83$ and $Ra = 5 \times 10^5$. The steady state distribution of the temperature field θ and the azimuthal velocity field ϕ in the mid cross section of the spherical shell obtained for both cases are shown in Fig. 11.

Clearly, the proximity of the internal baffle to any of the spherical shell boundaries suppresses the convective flow motion in the corresponding internal layer. In contrast, convective heat transfer with a fully developed thermal plume dominates in both cases in the wide internal layer. Also remarkable is an existence of the different shape patterns in the sub-layers of different widths for both cases: a crescent eddy in the narrow sub-layer and a modified kidney shape eddy in the wide sub-layer. The differences between all the configurations discussed were quantified in terms of *Nu* numbers, as summarized in Table 5. It is noteworthy that the most significant variation (−15% to +16%) of the *Nu* value was observed inside the non-equi-spaced spherical shell configuration. In this case, the minimal *Nu* value was provided by the smallest distance between the hot wall and the internal baffle, clearly indicating a route for further improvement of the spherical shell insulation efficiency. In contrast, the eccentricity of the internal baffle (both horizontal and vertical) has a much less pronounced effect on the heat flux rate through the boundaries of the spherical shell.

Table 5
Nu number values for a double-layered horizontally eccentric internal sphere.

Horizontal eccentricity ϵ	*Nu* number	Comparison with equi-spaced 3*w* configuration (*Nu* = 2.87)
0.167	2.92	+2%
0.335	2.89	+1%
Vertical eccentricity ϵ	*Nu* number	Comparison with equi-spaced 3*w* configuration (*Nu* = 2.87)
−0.335	3.16	+9%
0.335	3.15	+9%
D_b/D_i	*Nu* number	Comparison with equi-spaced 3*w* configuration (*Nu* = 2.87)
1.17	2.43	−15%
1.83	2.45	+16%

5. Conclusions

Laminar natural convection flow inside spherical shells with concentric, eccentric, equi-spaced and non-equi-spaced zero thickness internal baffles was investigated by the IBM. Numerical simulations were performed by extending the general pressure–velocity segregated solver [19] (based on the tensor product factorization (TPF) method combined with the Thomas solver (TPT)) with the immersed boundary functionality. The results obtained were extensively verified by performing detailed grid independence study and comparison with previously published data.

The insulation efficiency of the spherical shell was studied for up to five walls, corresponding to four equi-spaced concentric internal layers. It was found that the number of internal baffles has a considerable effect on the average *Nu* number, whose value computed for a shell with four equi-spaced concentric internal layers decreased by up to fourfold compared to that obtained for a single-layer spherical shell. It was shown that the length scale of the flow is determined by the difference between two adjacent walls. This observation allowed to derive a unified functional dependency correlating the modified Nu^* and Ra^* numbers for a spherical shell with up to four equi-spaced concentric internal layers. The effect of the eccentricity of the internal baffle (both horizontal and vertical) on the developing various flow patterns and on the insulating efficiency of a spherical shell was also investigated. The results – both qualitative and quantitative – showed that, for a particular *Ra*, both vertical and horizontal eccentricities have a quite limited impact on the total heat flux rate through the shell boundaries. In addition, the effect of the width of the internal layer and its proximity to the hot and cold boundaries on the total heat flux rate was studied. It was found that the configuration with the narrowest concentric layer close to the hot boundary provided the best insulating efficiency, characterized by a *Nu* value, that was about 15% lower than that obtained for the same operating conditions for the equi-spaced spherical shell. In contrast, the *Nu* for the spherical shell with the narrowest layer close to the cold boundary was about 16% higher than that of the equi-spaced spherical shell.

Conflict of interest

None declared.

References

[1] E.H. Bishop, S. Kolflat, L.R. Mack, J.A. Scanlan, Convective heat transfer between concentric spheres, in Proceedings of the heat transfer and fluidmechanics institute, Stanford University Press, Palo Alto, CA, USA, 1964.

[2] E. Bishop, L. Mack, J. Scanlan, Heat transfer by natural convection between concentric spheres, Int. J. Heat Mass Transfer 9 (1966) 649–652.

[3] L. Mack, H. Hardee, Natural convection between concentric spheres at low Rayleigh numbers, Int. J. Heat Mass Transfer 11 (1968) 387–396.

[4] J. Scanlan, E. Bishop, R. Powe, Natural convection heat transfer between concentric spheres, Int. J. Heat Mass Transfer 13 (1970) 1857–1872.

[5] S. Yin, R. Powe, J. Scanlan, E. Bishop, Natural convection flow patterns in spherical annuli, Int. J. Heat Mass Transfer 16 (1973) 1785–1795.

[6] T. Fujii, T. Honda, M. Fujii, Natural convection flow patterns in spherical annuli, Numer. Heat Transf. 7 (1984) 103–111.

[7] M. Fujii, H. Takamatsu, T. Fujii, A numerical analysis of free convection around an isothermal sphere (effects of space and Prandtl number), in: Proceedings 1987 ASME-JSME thermal engineering joint conference, Honolulu, Hawaii, USA, pp. 55–60.

[8] C. Chiu, W. Chen, Transient natural convection heat transfer between concentric and vertically eccentric spheres, Int. J. Heat Mass Transfer 39 (1996) 1439–1452.

[9] V. Travnikov, K. Eckert, S. Odenbach, Influence of the Prandtl number on the stability of convective flows between non-isothermal concentric spheres, Int. J. Heat Mass Transfer 66 (2013) 154–163.

[10] V. Travnikov, K. Eckert, S. Odenbach, Linear stability analysis of the convective flow in a spherical gap with $\eta = 0.714$, Int. J Heat Mass Transfer 80 (2015) 266–273.

[11] R. Powe, R. Warrington, J. Scanlan, Heat transfer by natural convection between concentric spheres, Int. J. Heat Mass Transfer 23 (1980) 1337–1350.

[12] B. Futterer, A. Brucks, R. Hollerbach, C. Egbers, Thermal blob convection in spherical shells, Int. J. Heat Mass Transfer 50 (2007) 4079–4088.

[13] A. Samanta, D. Appelo, T. Colonius, J. Nott, J. Hall, Computational modeling and experiments of natural convection for a titan mongolfiere, AIAA J. 48 (2010) 1007–1016.

[14] Yuri Feldman, Tim Colonius, Michael T. Pauken, Jeffrey L. Hall, Jack A. Jones, Simulation and cryogenic experiments of natural convection for the Titan Montgolfiere, AIAA Journal 50 (11) (2012) 2483–2491, http://dx.doi.org/10.2514/1.J051672.

[15] Y. Feldman, T. Colonius, On a transitional and turbulent natural convection in spherical shells, Int. J. Heat Mass Transfer 64 (2013) 514–525.

[16] C. Peskin, Flow patterns around heart valves: a numerical method, J. Comput. Phys. 10 (1972) 252–271.

[17] K. Taira, T. Colonius, The immersed boundary method: a projection approach, J. Comput. Phys. 225 (2007) 3121–3133.

[18] A. Roma, C. Peskin, M. Berger, An adaptive version of the immersed boundary method, J. Comput. Phys. 153 (1999) 509–534.

[19] H. Vitoshkin, A.Y. Gelfgat, On direct inverse of stokes, helmholtz and laplacian operators in view of time-stepper-based newton and arnoldi solvers in incompressible CFD, Commun. Comput. Phys. 14 (2013) 1103–1119.

[20] J. Mohd-Yusof, Combined immersed-boundary/b-spline methods for simulations of flow in complex geometries, center for turbulence research, Ann. Res. Briefs (1997) 317–327.

[21] A. Faldun, E.R. Verzicco, P. Orlandi, J. Mohd-Yusof, Combined immersed-boundary finite-difference methods for three-dimensional complex flow simulations, J. Comput. Phys. 161 (2000) 35–60.

[22] S.V. Patankar, Numerical Heat Transfer and Fluid Flow, McGraw-Hill, 1980.

[23] W. Ren, C. Shu, J. Wu, W. Yang, Boundary condition-enforced immersed boundary method for thermal flow problems with dirichlet temperature condition and its applications, Comput. & Fluids 57 (2013) 40–51.

[24] W. Ren, C. Shu, W. Yang, An efficient immersed boundary method for thermal flow problems with heat flux boundary conditions, Int. J. Heat Mass Transfer 64 (2013) 694–705.

[25] T. Kempe, J. Fröhlich, An improved immersed boundary method with direct forcing for the simulation of particle laden flows, J. Comput. Phys. 231 (2012) 3663–3684.

[26] T. Kempe, M. Lennartz, S. Schwarz, J. Fröhlich, Imposing the free-slip condition with a continuous forcing immersed boundary method, J. Comput. Phys. 282 (2015) 183–209.

[27] A.U. Gelfgat, Stability of convective flows in cavities: Solution of benchmark problems by a low-order finite volume method, Int. J. Numer. Methods Fluids 53 (2007) 485–506.

[28] H. Yoon, D. Yu, M. Ha, Y. Park, Three-dimensional natural convection in an enclosure with a sphere at different vertical locations, Int. J. Heat Mass Transfer 53 (2010) 3143–3155.

[29] A. Dehghan, K. Masih, Numerical simulation of buoyancy-induced turbulent flow between two concentric isothermal spheres, Heat Transfer Eng. 31 (2010) 33–44.

[30] H. Chu, T. Lee, Transient natural convection heat transfer between concentric spheres, Int. J. Heat Mass Transfer 36 (1993) 3159–3170.